frontiers | Frontiers in Earth Science

TYPE Original Research
PUBLISHED 29 December 2023
DOI 10.3389/feart.2023.1321488

OPEN ACCESS

EDITED BY
Jingbin Wang,
SINOPEC Petroleum Exploration and Production Research Institute, China

REVIEWED BY
Taohua He,
Yangtze University, China
Li Tian,
China University of Geosciences Wuhan, China

*CORRESPONDENCE
Bi Zhu,
zhubi@hhu.edu.cn
Chenhui Liu,
chliu@qnlm.ac

RECEIVED 14 October 2023
ACCEPTED 27 November 2023
PUBLISHED 29 December 2023

CITATION
Zhu B, Guo T, Liu C, Pan W, Chen Y, Zhang Y and Yang T (2023), Coastal upwelling and redox variations in the northwestern Tarim Basin (northwest China) during the Middle-Late Ordovician: implication for paleo-depositional conditions of the organic matter enrichment in the Saergan Formation.
Front. Earth Sci. 11:1321488.
doi: 10.3389/feart.2023.1321488

Coastal upwelling and redox variations in the northwestern Tarim Basin (northwest China) during the Middle-Late Ordovician: implication for paleo-depositional conditions of the organic matter enrichment in the Saergan Formation

Bi Zhu[1]*, Tingting Guo[1], Chenhui Liu[2]*, Wenqing Pan[3], Yongquan Chen[3], Yinggang Zhang[4,5] and Tao Yang[4]

[1]Institute of Earth's Critical Zone, School of Earth Sciences and Engineering, Hohai University, Nanjing, China, [2]Center for Isotope Geochemistry and Geochronology, Qingdao National Laboratory for Marine Science and Technology, Qingdao, China, [3]Research Institute of Exploration and Development, Tarim Oil Field Company, PetroChina, Korla, China, [4]State Key Laboratory for Mineral Deposits Research, Nanjing University, Nanjing, China, [5]State Key Laboratory of Palaeobiology and Stratigraphy, Nanjing Institute of Geology and Palaeontology, Chinese Academy of Sciences, Nanjing, China

The black shales of the Saergan Formation, which represent one of the main hydrocarbon source rocks in the Tarim Basin, witnessed a time span of organic matter enrichment by profound changes in the Earth System. A multi-proxy geochemistry study was carried out on the samples of the Saergan Formation to reconstruct the depositional environment and to explore the mechanism of organic matter enrichment of the unit at the Yingshanbeipo section, Keping area, northwest Tarim. Elemental and TOC data are suggestive of an upwelling setting, with a less pronounced oxygen minimum zone (OMZ) compared to the highly productive Peru and Namibian margins. Ferruginous anoxic bottom water conditions prevailed during most time of the deposition, with suboxic conditions dominating the basal and the top parts of the studied unit. As a whole, primary productivity seems to be the dominating factor that controlled the micronutrients and OM accumulations in the Saergan Formation whereas the role of benthic redox conditions may have been subordinate. The variations in primary productivity and bottom water redox conditions were resulted by the multiple, interacting environmental factors including nutrient supply regulated by oceanic circulation and climate changes, and relative sea-level fluctuations.

KEYWORDS

black shale, productivity, redox conditions, source rock, paleo-ocean

1 Introduction

Middle-Late Ordovician witnessed profound biodiversity known as the Great Ordovician Biodiversification (GOBE; Webby et al., 2004; Servais and Harper, 2018). Accompanied by the biological innovations, dramatic environmental changes had greatly shaped the Earth System during this time interval. These changes include the rise in atmospheric oxygen (e.g., Edwards et al., 2017; Krause et al., 2018), sustained cooling of the global ocean (Trotter et al., 2008), and the deposition of globally distributed organic-rich shales like the Athens Shale in North America, the Miaopo Formation on the Yangtze Platform in south China, the Pingliang Formation the north China, as well as the Saergan Formation in the Tarim Basin, northwest China (e.g., Bergström et al., 2000; Munnecke et al., 2011; Chen et al., 2017).

The Saergan Formation represents one of the most important hydrocarbon source rocks in the Tarim Basin (e.g., Liang et al., 2000; Gao et al., 2010; He et al., 2023). A number of paleontological, paleogeographical and geochemical studies have been carried out on this organic-rich interval (e.g., Zhao et al., 2006; Chen et al., 2012; Gao et al., 2012; Ma et al., 2013; Zhang and Munnecke, 2016; Liu C. et al., 2019; Ma et al., 2020; Li et al., 2022; Peng et al., 2023). However, less attention has been paid to the conditions responsible for the organic matter (OM) enrichment and paleo-oceanic conditions during the deposition.

The formation of organic-rich sediments is usually ascribed to the occurrence of oxygen-deficient conditions that favors OM preservation (e.g., Demaison and Moore, 1980) or high primary production that enhances OM flux to the ocean floor (e.g., Calvert and Price, 1983; Pedersen and Calvert, 1990). Additional factors including sea level fluctuations, climatic conditions, and oceanic circulation may also influence the sequestration and preservation of OM (Sageman et al., 2003; Tyson, 2005). In fact, in many cases, the development of organic-rich sediments may link to multiple, interacting factors and may vary among diverse sedimentary environments (Sageman et al., 2003; Rimmer et al., 2004; Lu et al., 2019; Gao et al., 2021) Therefore, to better understand the influences of these factors on OM accumulation in the Saergan Formation, a comprehensive geochemical study is needed to reconstruct the depositional conditions of the Saergan Formation against a backdrop of distinct environmental changes in the Middle-Late Ordovician.

In this study, we present a multi-proxy study of the Saergan Formation of the Yingshanbeipo section in northwest Tarim, with the aim to explore the depositional history, as well as mechanisms of OM accumulation and preservation of the sedimentary succession. Approaches including redox proxies (iron speciation, redox-sensitive elements), primary productivity proxies (micro-nutrients, TOC), and terrigenous flux proxies (Al, Ti, Zr/Al) were employed to constrain the redox variation, sea level change, primary productivity, and their interplay during deposition of the organic-rich interval.

2 Geological setting

The Tarim Basin in northwestern China represents one of the major continental blocks in China. This block is bound by the Tianshan mountain belt to the north, and the west Kunlun and central-Southern Altyn Tagh mountain belts to the southwest and southeast, respectively (Figure 1). In the Middle-Late Ordovician, the Tarim block was located at low latitudes, comprising four submarine depressions (Jia et al., 2004; Lin et al., 2012; Figures 1A, B). The Keping area was located at the western end of the Central High (Figures 1B, C). Ordovician sedimentary outcrops are scattered in this area and comprises the Lower Ordovician Penglaiba and Yingshan formations, the Middle Ordovician Dawangou and Saergan formations, and the Upper Ordovician Kanling, Qilang and Yingan formations in ascending order. The Saergan Formation, which serves as one of the most important hydrocarbon source rocks in the Tarim Basin, is distributed along a southwest-northeast belt in the Keping-Aksu area (Gao et al., 2010). The Keping area was traditionally interpreted to represent an upper slope facies during the Middle-Late Ordovician, but recent studies have suggested that it may not have been a normal slope setting but part of a large intraplatform basin that originated from a depression formed overlying the Dawangou dolomitic limestone (Chen et al., 2012; Ma et al., 2013), or part of a gulf with its west end connecting to the open ocean (Gao et al., 2016).

The Yingshanbeipo section is located ca. 50 km northeast of the Keping county town. In the Yingshanbeipo section, the Dawangou, Saergan, and Kanling Formations can be observed. The Dawangou Formation is composed of grey, thin-bedded limestone, and the Saergan Formation is dominated by black shale intercalated with thin-bedded and lenticular limestone. The Saergan Formation is further overlain by the grey-purple, carbonate-dominating Kanling Formation (Figure 1D). According to palaeontological data from the adjacent Dawangou section (ca. 5 km southwest of Yingshanbeipo), the Saergan Formation bears abundant planktonic fossils including graptolite, acritarch, and chitinozoan. Four graptolite zones (the *Pterograptus elegans*, the *Didymograptus murchisoni*, the *Dicellograptus vagus*, and the *Nemagraptus gracilis* biozones) and two conodont biozones (the *Pygodus serra* and the *Pygodus anserinus* biozones) were recognized in the Saergan Formation, which constrained the age of the Saergan Formation from middle Darriwilian to early Sanbian (Zhen et al., 2011; Chen et al., 2012).

3 Materials and methods

Twenty three black shale samples were collected from the Saergan Formation of the Yingshanbeipo section and their stratigraphic heights are listed in Table 1.

For trace elements analysis, about 50 mg sample powders were weighed into a Teflon beaker and digested using a mixture of concentrated HNO_3 and HF. To ensure complete digestion, the beaker was capped, placed in a steel jacket, and then heated in an oven for 72 h at 190°C. The obtained solution was dried and re-dissolved in concentrated HNO_3 for another 12 h at 120°C. Finally, the solution was diluted and Rh was added as an internal standard. Following this, the trace metals abundances were measured using an HR-ICP-MS (Element XR, Thermo Fisher) and the analytical precision was better than 5%.

For iron speciation analysis, a sequential extraction method was used to extract different iron fractions. The sequential extraction method is a combination of Poulton and Canfield, (2005); Huerta-

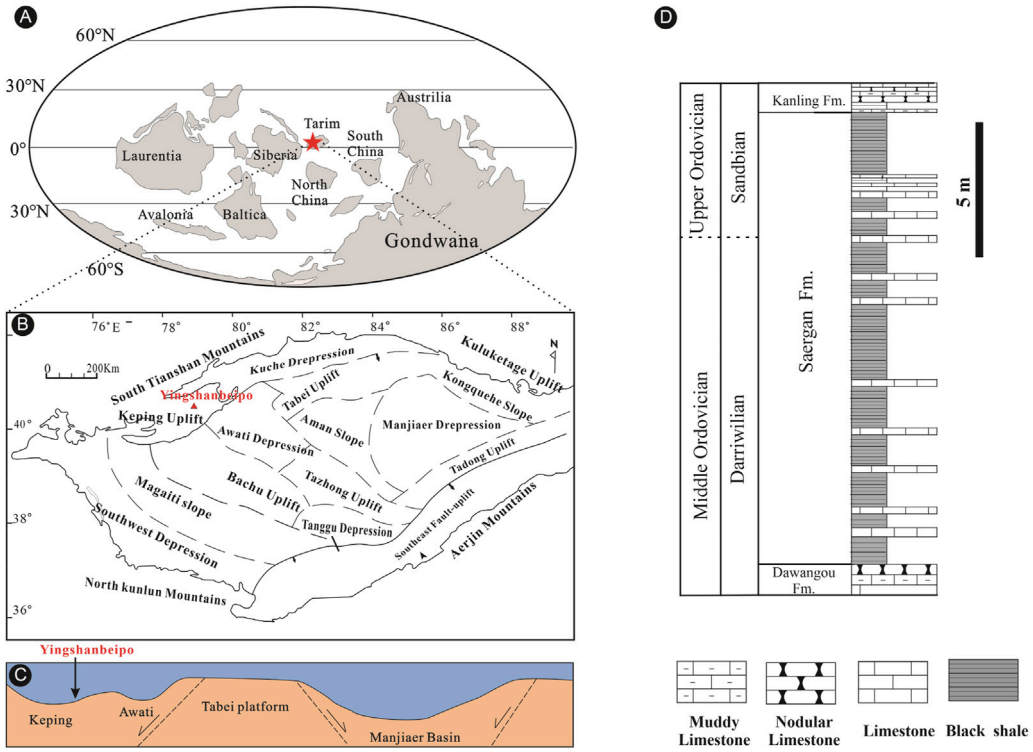

FIGURE 1
(A) Palaeogeographic reconstruction of the Middle-Late Ordivician (~460 Ma) (after Torsvik and Cocks, 2013). **(B)** Structure diagram of he Tarim Basin showing the position of the studied section (Yang et al., 2020). **(C)** Smplified profile across the Tarim Basin showing the paleobathymetric position of the studied section in the Ordovician (after Zhang and Munnecke, 2016; Yang et al., 2020). **(D)** Generalized stratigraphy of the Yingshangbeipo section.

Diaz and Morse (1990) and has been employed in previous studies (e.g., Ding et al., 2014; Liu C. et al., 2019). The details of the extraction procedure have been described in Liu M. et al. (2019) and are briefly outlined here. For each sample, about 100 mg of powdered sample was weighed. The iron fraction associated with carbonate (Fe_{carb}) was extracted using 10 mL of 1 mol L^{-1} sodium acetate (adjusted to PH 4.5) with 48 h of shaking at 50°C. After the supernatant was removed, 10 mL of 50 g L^{-1} sodium dithionite and 0.2 mol L^{-1} tri-sodium citrate (buffered to PH 4.8) were added to the residue. The mixture was shaken for 2 h at room temperature to extract the iron fraction of ferric (hydro)oxides (Fe_{ox}). Afterwards, the magnetite fraction (Fe_{mag}) was extracted by adding 10 mL of 0.2 mol L^{-1} ammonium oxalate and 0.17 mol L^{-1} oxalic acid (PH = 3.2) with 6 h of shaking at room temperature. Following this, the silicates-bonding iron (Fe_{sil}) was extracted using 10 mL of 10 mol L^{-1} Hyfrofluoric acid with 24 h shaking at room temperature with adding 2.0 g of Boric acid after16 h. Finally, 10 mL of concentrated HNO_3 was added to dissolve the pyrite iron (Fe_{Py}) at room temperature (shaking for 2 h). Each obtained solution was analyzed for Fe and Al concentrations using an ICP-OES (ICP-3000, Skyray) and the precision was better than 5%. Total Fe (Fe_T) and Al were calculated as the sum of the Fe and Al concentrations of the five solutions. Fe_{HR} is defined as the sum of Fe_{carb}, Fe_{ox}, Fe_{mag} and Fe_{Py}, and Fe_U represents the unreactive iron and equals to Fe_{sil}.

Excess 2 mol L^{-1} hydrochloric acid was added to each sample to make sure all the carbonate fractions were dissolved. Afterwards, the solid residue was rinsed, dried, and Homogenized. TOC values were then analyzed on an Element Analyzer (Vario Macro, Elemantar). Analytical error was better than 0.1%.

Trace elemental, iron speciation, and Al analyses were performed at the State Key Laboratory for Mineral Deposits Research, Nanjing University. TOC analysis was performed at Key Laboratory of Surficial Geochemistry, Ministry of Education, Nanjing University.

4 Results

All geochemical data from the Yingshanbeipo section including trace elements, TOC, Al, and iron speciation data are listed in Table 1. Enrichment factors (EFs) of trace elements are calculated against the values of Post-Archean average Australian shale (PAAS, Taylor and Mclennan, 1985) using $X_{EF} = (X/Al)_{sample}/(X/Al)_{PAAS}$ where X is the element of interest.

The Fe_T values of the Yingshanbeipo samples range from 0.70% to 2.98% (average = 1.73%), all larger than 0.5%, supporting the validity of the iron speciation data (Clarkson et al., 2014). Fe_U ranges from 0.14% to 1.60% (average = 0.89%). The Fe_{HR}/Fe_T ratios ranges from 0.25 to 0.80 (average = 0.52). Two samples from the top and the bottom exhibit low Fe_{HR}/Fe_T ratios of 0.22 and 0.38, respectively, while the rest samples yield Fe_{HR}/Fe_T ratios above the threshold of 0.38 characterizing anoxic sediments (Poulton and Canfield, 2011). The Fe_{Py}/Fe_{HR} ratios of the sample subset with Fe_{HR}/Fe_T >0.38 are

TABLE 1 Iron speciation, trace elements and Al data of the Saergan Formation at the Yingshanbeipo section, Northwest Tarim.

Sample id	Depth (m)	Mn (ppm)	Ti (ppm)	V (ppm)	Co (ppm)	Ni (ppm)	Cu (ppm)	Zn (ppm)	Mo (ppm)	U (ppm)	Zr (ppm)	Al (wt%)	Fe (wt%)	Fe_{HR} (wt%)	Fe_{HR}/Fe_T	Fe_{py}/Fe_{HR}
SA-01	0.8	172.2	9,513.0	71.4	17.2	50.0	48.2	78.7	1.3	12.3	122.7	6.4	2.2	0.8	0.37	0.01
SA-02	1.0	117.7	11,043.3	67.7	38.0	57.6	29.6	94.2	1.2	4.2	123.3	6.0	2.3	1.0	0.44	0.01
SA-03	2.2	153.0	10,742.9	162.7	56.9	102.0	122.6	112.9	2.7	9.3	112.8	5.2	1.8	1.0	0.53	0.01
SA-04	2.3	125.7	8,792.6	101.1	18.1	70.8	108.6	72.0	3.2	9.8	102.1	5.7	2.2	1.1	0.49	0.01
SA-05	2.5	139.2	7,276.2	139.8	61.8	85.8	87.0	90.1	2.0	9.7	77.5	3.9	1.4	0.8	0.62	0.01
SA-06	3.0	164.0	8,463.0	96.4	29.7	68.9	93.8	68.9	1.6	8.7	93.3	4.1	1.3	0.6	0.47	0.01
SA-07	4.0	146.8	4,906.5	71.5	208.6	65.2	72.3	83.7	2.1	5.4	54.7	2.9	1.1	0.8	0.76	0.01
SA-08	4.5	145.6	10,068.7	117.8	27.9	63.8	81.3	102.0	1.9	10.9	105.2	4.9	1.5	0.8	0.53	0.01
SA-09	6.0	133.3	3,213.3	118.8	54.6	100.7	118.1	100.7	2.5	9.6	76.0	4.2	1.4	0.8	0.56	0.01
SA-10	7.9	128.9	4,813.3	50.8	32.2	42.7	48.5	53.9	1.3	5.0	55.1	3.2	1.0	0.5	0.48	0.01
SA-11	8.4	124.0	4,082.6	82.9	28.1	85.3	112.1	92.6	2.4	10.1	72.3	4.3	1.6	0.9	0.52	0.01
SA-12	8.7	104.2	2,005.3	89.2	11.3	73.4	65.1	63.5	1.7	7.7	63.7	3.8	1.3	0.6	0.48	0.01
SA-13	9.0	159.3	1,054.3	47.6	141.6	33.0	19.4	32.5	1.8	1.9	13.4	1.2	0.8	0.7	0.80	0.04
SA-14	9.2	105.5	4,904.0	68.0	25.8	56.1	71.9	68.9	2.2	5.6	55.6	3.1	1.1	0.6	0.52	0.01
SA-15	9.7	191.4	1,445.4	59.0	250.4	44.7	28.4	44.9	2.6	2.6	17.3	1.0	0.7	0.6	0.80	0.05
SA-16	10.2	116.7	7,998.1	186.7	22.7	103.0	111.9	115.5	5.8	6.8	105.8					
SA-17	10.6	145.9	8,769.3	163.0	13.3	114.6	118.9	127.2	5.1	10.3	110.1	6.7	2.6	1.2	0.46	0.01
SA-18	11.0	267.2	10,891.0	211.5	25.4	119.1	127.9	150.7	3.4	12.0	127.1	5.3	2.0	0.9	0.44	0.01
SA-19	12.0	174.2	10,531.3	297.2	31.2	107.5	118.3	139.2	6.6	10.0	123.6	7.1	3.0	1.5	0.51	0.01
SA-20	12.2	373.8	16,606.5	202.2	34.4	136.5	166.3	206.2	3.0	17.2	179.6	6.1	2.3	1.0	0.44	0.01
SA-21	12.7	239.9	5,205.4	209.8	23.2	129.1	144.1	164.7	4.1	22.3	142.4	5.0	2.2	1.0	0.47	0.01
SA-22	13.6	273.4	9,477.1	114.3	29.6	67.9	77.7	95.5	1.2	7.4	108.1	5.9	2.1	0.9	0.43	0.01
SA-23	14.1	362.3	10,800.4	134.5	17.5	86.4	96.3	106.7	1.0	9.5	131.3	6.3	2.1	0.5	0.25	0.02

Sample id	Depth (m)	Fe_U (wt%)	TOC (%)	V_{EF}	Mn_{EF}	Co_{EF}	Ni_{EF}	Mo_{EF}	U_{EF}	Zn_{EF}	Cu_{EF}	Zr/Al	Co_{EF}*Mn_{EF}	Co(ppm)*Mn(%)
SA-01	0.8	1.36	0.08	0.75	0.32	1.18	1.43	2.05	6.23	1.46	1.52	19.29	0.37	2.97
SA-02	1.0	1.28	0.11	0.75	0.23	2.76	1.75	1.99	2.26	1.85	0.99	20.58	0.64	4.47

(Continued on following page)

10.3389/feart.2023.1321488

TABLE 1 (*Continued*) Iron speciation, trace elements and Al data of the Saergan Formation at the Yingshanbeipo section, Northwest Tarim.

Sample id	Depth (m)	Fe_U (wt%)	TOC (%)	V_{EF}	Mn_{EF}	Co_{EF}	Ni_{EF}	Mo_{EF}	U_{EF}	Zn_{EF}	Cu_{EF}	Zr/Al	Co_{EF}*Mn_{EF}	Co(ppm)*Mn(%)
SA-03	2.2	0.86	0.47	2.09	0.35	4.76	3.57	5.19	5.76	2.56	4.72	21.69	1.64	8.70
SA-04	2.3	1.12	1.70	1.18	0.26	1.38	2.26	5.59	5.55	1.49	3.81	17.90	0.36	2.28
SA-05	2.5	0.52	1.54	2.38	0.42	6.85	3.98	5.17	7.98	2.70	4.44	19.75	2.85	8.60
SA-06	3.0	0.70	1.14	1.55	0.46	3.12	3.02	3.88	6.75	1.95	4.53	22.49	1.45	4.87
SA-07	4.0	0.26	1.21	1.62	0.59	30.80	4.03	7.08	5.96	3.34	4.91	18.55	18.02	30.61
SA-08	4.5	0.72	0.80	1.59	0.35	2.45	2.35	3.75	7.13	2.43	3.29	21.30	0.85	4.06
SA-09	6.0	0.63	1.15	1.91	0.38	5.72	4.40	5.96	7.49	2.85	5.69	18.27	2.15	7.28
SA-10	7.9	0.52	0.77	1.07	0.48	4.41	2.45	4.12	5.11	2.00	3.06	17.34	2.10	4.16
SA-11	8.4	0.78	0.87	1.29	0.34	2.85	3.61	5.52	7.57	2.54	5.23	16.86	0.97	3.49
SA-12	8.7	0.66	1.40	1.57	0.32	1.30	3.52	4.56	6.56	1.97	3.43	16.78	0.42	1.18
SA-13	9.0	0.17	0.93	2.69	1.58	52.11	5.08	15.14	5.11	3.23	3.29	11.31	82.45	22.55
SA-14	9.2	0.52	1.12	1.44	0.39	3.57	3.24	6.96	5.70	2.58	4.57	17.67	1.41	2.72
SA-15	9.7	0.14	0.93	3.83	2.19	106.15	7.93	25.22	8.30	5.15	5.54	16.89	232.45	47.93
SA-16	10.2		1.30											2.65
SA-17	10.6	1.38	1.30	1.61	0.25	0.86	3.10	7.57	4.95	2.22	3.53	16.35	0.22	1.94
SA-18	11.0	1.12	1.52	2.64	0.59	2.07	4.06	6.35	7.27	3.32	4.79	23.80	1.22	6.79
SA-19	12.0	1.47	1.18	2.81	0.29	1.92	2.77	9.30	4.56	2.32	3.35	17.49	0.56	5.43
SA-20	12.2	1.29	1.19	2.20	0.71	2.44	4.04	4.87	9.04	3.95	5.42	29.24	1.74	12.86
SA-21	12.7	1.20	1.88	2.78	0.56	2.00	4.66	8.08	14.29	3.85	5.72	28.24	1.12	5.55
SA-22	13.6	1.17	1.10	1.30	0.55	2.19	2.10	2.12	4.07	1.91	2.65	18.39	1.20	8.10
SA-23	14.1	1.60	1.14	1.42	0.67	1.21	2.49	1.64	4.87	1.99	3.06	20.83	0.82	6.34

10.3389/feart.2023.1321488

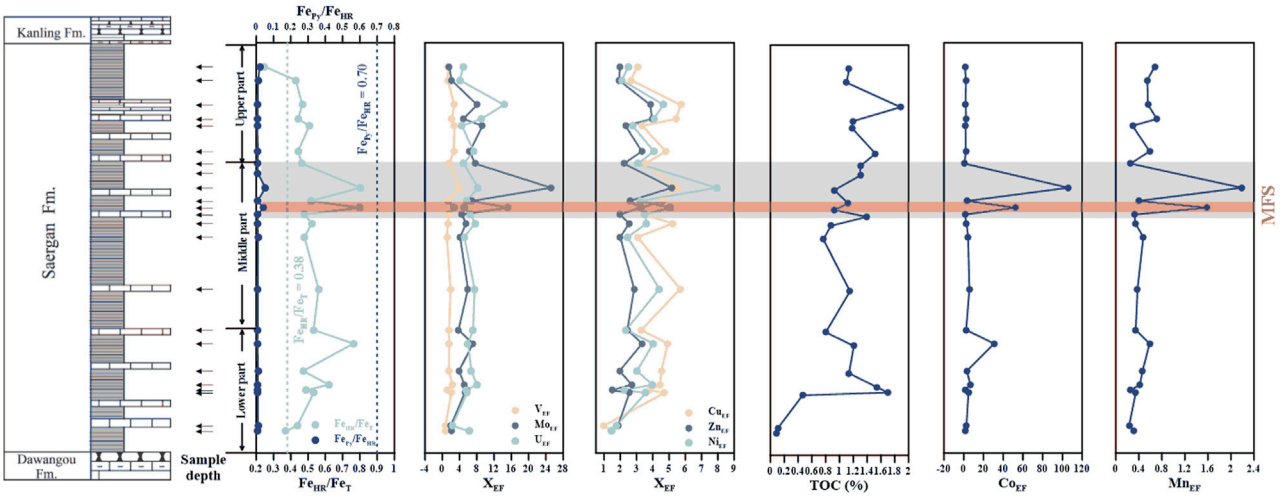

FIGURE 2
Vertical profiles of redox proxies, primary productivity proxies, Co_{EF} and Mn_{EF} of the Saergan Formation in the Yingshanbeipo section (MFS, maximum flooding surface). The shaded area represents maximum anoxia during deposition (see the text for more details).

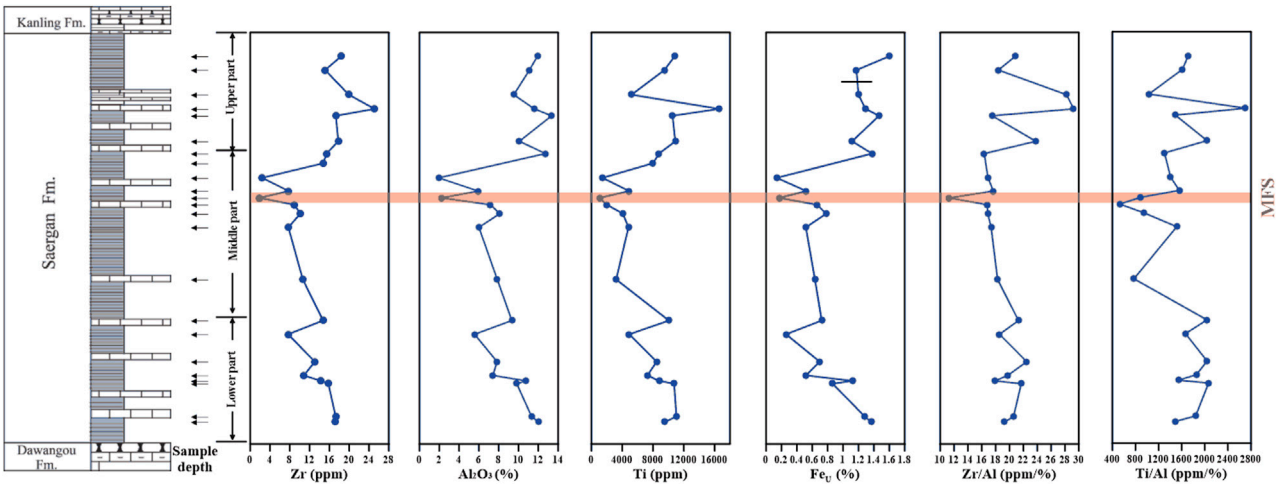

FIGURE 3
Vertical profiles of detrital input proxies of the Saergan Formation in the Yingshanbeipo section (MFS, maximum flooding surface).

generally low (0.01–0.05; average = 0.01), indicating anoxic and ferruginous bottom water conditions (Poulton and Canfield, 2011).

For redox-sensitive elements, Mo ranges from 1.03 to 6.57 ppm (average = 2.63 ppm) with Mo_{EF} ranging from 1.64 to 25.22 (average = 6.46); U ranges from 1.87 to 22.32 ppm (average = 9.06 ppm) with U_{EF} ranging from 2.26 to 14.29 (average = 6.48); V ranges from 47.63 to 297.20 ppm (average = 124.52 ppm) with V_{EF} ranging from 0.75 to 3.83(average = 1.84). The Mo_{EF} values exhibit a gradual increase in Mo_{EF} with some fluctuations in the lower part and maintains relatively invariant upsection (Figure 2). An abrupt increase in Mo_{EF} values is observed at the top of the middle part (shaded area in Figure 2), followed by a gradual decrease upsection. Similar variations are also observed for V_{EF} and U_{EF} but are less prominent than Mo_{EF} (Figure 2).

For nutrient trace metals (Ni, Cu, Zn), Ni ranges from 33.04 to 136.52 ppm (average = 81.05 ppm) with Ni_{EF} ranging from 1.43 to 7.93 (average = 3.45); Cu ranges from 19.42 to 166.34 ppm (average = 89.95 ppm) with Cu_{EF} ranging from 0.99 to 5.72 (average = 3.98); Zn ranges from 32.46 to 206.17 ppm (average = 98.49 ppm) with Zn_{EF} ranging from 1.46 to 5.15 (average = 2.62). The Ni_{EF}, Cu_{EF} and Zn_{EF} values are more fluctuated than that of EFs of Mo, U and V, and the maximum values are also located within the interval within which Mo, U and V show maximum EFs (Figure 2).

The concentrations of Al, Zr, and Ti range from 1.03% to 7.07% (average = 4.66%), 13.37–179.56 ppm (average = 94.46 ppm), and 1,054.28–16,606.47 ppm (average = 7,504.50 ppm), respectively. The vertical profiles of Al, Zr, and Ti are highly resembling, characterized by a gentle decrease in the lower part and a steeper

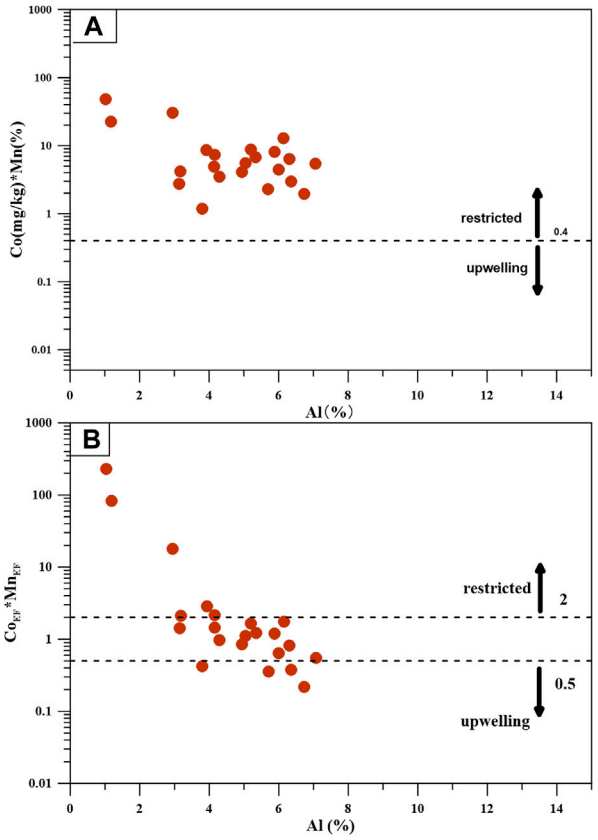

FIGURE 4
Co*Mn-Al **(A)** and Co_{EF}*Mn_{EF}-Al **(B)** diagrams of the Saergan Formation in the Yingshanbeipo Section (after Sweere et al., 2016).

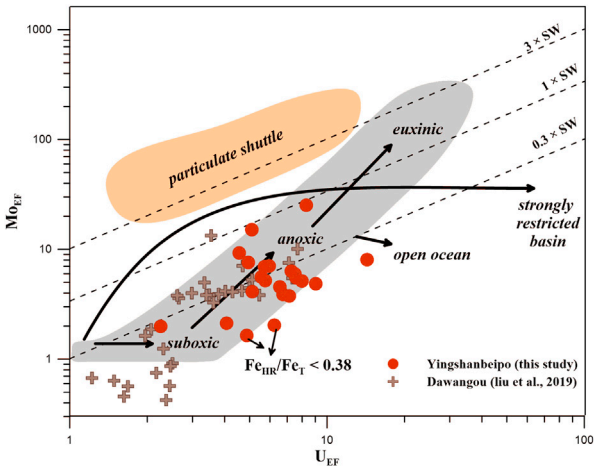

FIGURE 5
Mo-U diagram of the Saergan Formation in the Yingsanbeipo and the adjacent Dawangou sections. Redox fields and particulate shuttle are from Algeo and Tribovillard (2009). The dashed lines indicated multiples (0.3, 1, and 3) of the Mo/U ratios of the present-day seawater. The suboxic facies are defined as settings with low oxygen levels and favor use of oxidants other than O_2 in microbially mediated reduction reactions (Algeo and Li, 2020). Anoxic facies in this diagram are defined as anoxic-nonsulfidic (free of O_2 and H_2S) and euxinic facies are defined as settings with no O_2 but with the presence of free H_2S (Algeo and Li, 2020).

increase in the upper part (Figure 3). The nadirs in Al, Ti, and Zr contents are located at the interval where Mo_{EF} shows the maximum values (Figure 3). The Zr/Al profile is slightly different from those of Al, Ti, and Zr, yet exhibiting an overall decrease-increase pattern from bottom to top with larger fluctuations (Figure 3). In addition, the Fe_U values, which represent the Fe fraction linked to silicates, also follows a decrease-increase pattern (Figure 3).

In order to evaluate the hydrographic conditions (upwelling vs. basin restriction) during deposition of the Saergan Fm at Yingshanbeipo, we calculated the Co*Mn and Co_{EF}*Mn_{EF} values of the studied samples. The Co (ppm)*Mn (%) and Co_{EF}*Mn_{EF} values of the Yingshanbeipo samples vary between 1.18 to 47.93 and 0.22 to 232.45, respectively, higher than those from highly productive upwelling zones (Figure 4).

5 Discussion

5.1 Redox variations during deposition of the Saergan Formation

5.1.1 Iron speciation

Iron speciation and redox-sensitive elements (Mo, U, V) data are used to track the local redox conditions in the bottom waters of the Saergan Formation at Yingshanbeipo. The principle of iron speciation proxy is based on the redox-related redistribution of Fe in the ocean (Raiswell and Canfield, 1998; Wijsman et al., 2001). Generally, sediments in anoxic settings are characterized by the enrichment of highly reactive iron (Fe_{HR}) (e.g., Lyons and Severmann, 2006). Statistically, a ratio of reactive iron to total iron (Fe_{HR}/Fe_T) larger than 0.38 is typical of anoxic marine sediments, whereas Fe_{HR}/Fe_T <0.22 indicates oxic marine settings (Poulton and Canfield, 2011). Additionally, the speciation of Fe_{HR} can further distinguish different anoxic marine depositional conditions. The proportion of Fe_{HR} bound as sulfide (Fe_{py}/Fe_{HR}) exhibits ratios of >0.7 in euxinic depositional settings, whereas Fe_{py}/Fe_{HR} falls below 0.7 in ferruginous settings (free sufides are restricted mainly to porewaters) (Poulton and Canfield, 2011).

The iron speciation data indicate most of the studied samples, except for two samples from the top and the bottom, were deposited in anoxic and ferruginous bottom water conditions (Table 1; Figure 2). The two samples with low Fe_{HR}/Fe_T ratios yield values between 0.22 and 0.38, a range considered to be equivocal and could be indicative of oxic or anoxic settings (Poulton and Canfield, 2011). For the two samples, the redox conditions will be discussed in the following context (section 5.1.2).

5.1.2 Redox-sensitive elements (Mo, U, V)

Redox-sensitive elements like U, Mo, and V can provide useful information on paleoredox conditions of marine sediments. In oxic seawater, Mo, U, and V behave conservatively in the form of MoO_4^{2-}, U^{6+}, and V^{5+}, respectively (Tribovillard et al., 2006). When certain redox thresholds are reached, the metals are reduced and can be further taken up in sediments. The reduction of U^{6+} to U^{4+} and V^{5+}

to V^{4+} initiate at the Fe^{3+} to Fe^{2+} transition (Morford and Emerson, 1999; Tribovillard et al., 2006). In contrast, the accumulation of authigenic Mo in marine sediments requires conditions with free H_2S, which favor the formation of reactive thimolybdate species (Helz et al., 1996; Erickson and Helz, 2000). The presence of free H_2S also enhances the reduction of U^{6+} to U^{4+} and leads to further reduction of V^{4+} to V^{3+}. Therefore, the accumulations of U and V are also promoted in euxinic facies (Tribovillard et al., 2006). Consequently, moderate enrichments of U or V with little or no Mo enrichment are generally indicative of suboxic conditions whereas co-enrichments of all three metals are typical of anoxic conditions (e.g., Algeo and Tribovillard, 2009; Tribovillard et al., 2012; Figure 5). When the bottom waters become euxinic, Mo, U and V are strongly enriched with the enrichment of Mo being most prominent (Algeo and Tribovillard, 2009; Tribovillard et al., 2006; Figure 5).

Recent studies addressed that caution must be taken when using U and V data as redox proxies, since the metals may both be influenced by the uptake via apatite precipitation (Lumiste et al., 2021). We consider the U and V enrichments observed in this study are unlikely to have a strong links to apatite. As shown in Lumiste et al. (2021), vertical profiles of U and V exhibit co-variations in the phosphorus-rich interval of the studied core, but the profile of Mo exhibits an opposite variation pattern in comparison to U and V (their Figure 4). For our data, opposite variation patterns were not observed between U(V) and Mo (Figure 2). Instead, covariation was found between U and Mo, and to a lesser extent, between V and Mo (Figure 2), indicating redox conditions rather than uptake by apatite precipitation was likely the main reason for the variations in the metals.

In the Mo_{EF}-U_{EF} diagram, the covariation patterns of the Yingshanbeipo samples cover a wide range extending from the suboxic to the anoxic ends (Figure 5). The lowest and the topmost samples with low Fe_{HR}/Fe_T ratios are plotted near the suboxic end, exhibiting little Mo enrichment but elevated U enrichment (Figure 5), suggesting they were likely deposited in suboxic conditions. Except for a few exceptions, the rest samples exhibit moderate enrichments in both U and Mo, consistent with the interpretation of predominately anoxic ferruginous conditions based on Fe speciation data. The vertical profiles of Mo_{EF} and U_{EF} also exhibit relatively low values at the base and the top (although this pattern is less prominent for V_{EF}) (Figure 2), supporting more oxic conditions for the basal and the topmost parts. Similarly, more oxic conditions were also observed both at the top and the bottom of the Saergan Formation in the adjacent Dawangou section (Liu C. et al., 2019). Taking together, the integrated redox-sensitive elements and iron speciation data indicate the redox conditions for the Saergan Formation at the Yingshanbeipo section were variable during its deposition, from suboxic at the lowermost interval, to anoxic ferruginous upsection, and to suboxic conditions at the top. The interval exhibiting concurrent peaks in the Mo_{EF}, V_{EF} as well as Fe_{HR}/Fe_T values in the upper Saergan Formation may correspond to the maximum anoxia during deposition (Figure 2).

The Mo-U data of the Saergan Formation from the adjacent Dawangou section were also plotted in Figure 5. The data are highly scattered and tend to show lower U_{EF} and Mo_{EF} values compared to the Yingshanbeipo samples. The differences in Mo-U patterns reflect that the Yingshanbeipo samples had been deposited in more reducing water mass conditions than the Dawangou samples. Previous studies have proposed that the sections may have been located on a steep slope dipping northeast (Figure 1), thus the Yingshanbeipo section northeast of Dawangou is likely to have deposited in deeper waters. Collectively, the differences in redox conditions of the two sections are likely to record heterogeneity in redox conditions of bottom waters, which probably link to different water depths.

5.2 Sea level changes

Chemostratigraphic characteristics of organic-rich marine sediments have the potential to track the transgression-regression cycles during deposition (LaGrange et al., 2020). Elements like Al, Ti, and Zr, which are predominately associated with detrital sediments, are used as proxies for the abundance of detrital input and further the identification of sequence stratigraphic surfaces (LaGrange et al., 2020 and references therein). For example, local minimum concentrations in terrigenous proxies are usually linked to the switch from transgression to regression for organic-rich sediments, whereas peaks in terrigenous proxies are generally associated with the regression-transgression transition (e.g., Turner et al., 2016; Harris et al., 2018). In addition, variations in elements ratios like Zr/Al and Ti/Al of marine sediments can also be used to track the relative sea level changes (e.g., LaGrange et al., 2020; Li et al., 2021). As Zr/Al and Ti/Al ratios may indicate the abundance of coarse sediments supply, minimum in those ratios in organic-rich units is considered to be a chemostratigraphic expression of the transgression-regression transition (LaGrange et al., 2020 and references therein).

There are different opinions regarding the depositional history of the Saergan Formation in the Keping area. Zhang and Munnecke (2016) proposed that the Saergan Formation may have been deposited during a significant transgression, or it may be deposited during a regression in a restricted setting. In the first scenario, a pronounced transgression drowned the pre-existing carbonate platform and the organic-rich Saergan Formation sediments were deposited. In the latter scenario, lowered sea level would have reduced the connectivity of the Keping region to the open ocean, leading to water stagnancy and oxygen depletion in bottom waters and finally the deposition of the Saergan Formation.

For our sample set, the vertical profiles of the terrigenous elements (Al, Zr, Ti), Fe_U, Zr/Al and Ti/Al ratios are highly resembling (Figure 3). The systematic vertical variations in the proxies indicate the deposition of the Saergan Formation corresponds to a marine transgression and subsequent regression. The maximum flooding surface is likely located within the upper part of the studied unit (Figure 3), as indicated by concurrent nadirs in terrigenous elemental contents, Fe_U, Zr/Al and Ti/Al ratios. Our data thus support the first scenario by Zhang and Munnecke. (2016) and contradict the regression model. Our interpretation is consistent with that of Gao et al. (2012), in which the gamma ray, Th/U, and Th/K data indicated the Saergan Formation corresponds to a third-order sequence of sea-level changes with the maximum flooding surface located at the upper part of the unit.

Changes in sea-level are known to have a major impact on the benthic redox conditions as higher sea level would reduce mixing

from oxic surface waters and may possibly lead to incursion of deep, oxygen-deleted waters (e.g., Jin et al., 2014; Harris et al., 2018). For our samples, the variations in redox proxies (Fe_{HR}/Fe_T, Mo_{EF}, U_{EF} and V_{EF}) are generally in step with the changes in sea-level (i.e., transition from suboxic to anoxic at the base with sea-level rise, the concurrent peaks in the Fe_{HR}/Fe_T, Mo_{EF}, U_{EF} and V_{EF} values near the inferred maximum flooding surface, and the transition to more oxic conditions towards the top with sea level fall). Although other factor may also have contributed to the redox variations (see section 5.5), sea-level changes represent an important factor in regulating the benthic redox conditions when the Saergan Fm. was deposited.

5.3 Upwelling and basin restriction

Coastal upwelling zones and restricted basins are both prone to the development of anoxic conditions and the accumulation of OM (Brumsack, 2006). It was proposed that the Saergan Formation in the studied region was developed in an ancient upwelling zone with high productivity (Liu M. et al., 2019). Meanwhile, as described in section 2, the Saergan Formation may also have been partially shielded from the open ocean, which raises the possibility of basin restriction during deposition. Previous studies have suggested that elemental data of sediments have the potential to differentiate between the two settings (e.g., Brumsack, 2006; Sweere et al., 2016; Zhang et al., 2018). For example, Ma et al. (2022) proposed that Co and Mn contents in carbonate-bearing fluorapatite (CFA) can be used to distinguish between lacustrine and open marine settings. Whole-rock analysis shows sediments in upwelling systems usually exhibit low Co and Mn contents in comparison to restricted settings. The differences were attributed to the systematic differences in the supply of Co and Mn to the water column. In upwelling systems, the supply of the two metals is driven by the upwelling of deeper oceanic waters that are deprived in Co and Mn (Brumsack, 2006; Sweere et al., 2016). Co and Mn concentrations are higher in sediments from restricted basins like the Black Sea. In restricted settings, the supply of Co and Mn is dominated by Co and Mn-rich river waters and restricted water has facilitated the build-up of higher Mn and Co concentrations (Morford and Emerson, 1999; Sarmiento and Gruber, 2006; Sweere et al., 2016). Consequently, typical upwelling settings display low Co (ppm)*Mn (%) (<0.4) and Co_{EF}*Mn_{EF} (<0.5) values while restricted settings exhibit elevated Co (ppm)*Mn (%) (>0.4) and Co_{EF}*Mn_{EF} (>2) values (Figure 4). Additionally, Cd/Mo ratio of sediment can also be used as an effective proxy to distinguish the two settings (Sweere et al., 2016). Cd is closely associated with primary productivity and exhibits a nutrient-like profile in seawater (Bruland, 1980; Conway and John, 2015). In highly productive upwelling settings, Cd is incorporated into plankton and can be efficiently transported into sediments via settling planktonic biomass. Consequently, sediments of highly productive upwelling zones feature pronounced Cd enrichment with higher Cd/Mo ratios (>0.1) while hydrographically restricted settings exhibit Cd/Mo <0.1 (Sweere et al., 2016). However, intermediated characteristics are found for settings that feature both upwelling and restriction (e.g., the Cariaco Basin) or upwelling zones with less pronounced OMZs like the Arabian Sea (Sweere et al., 2016).

The Co*Mn and Co_{EF}*Mn_{EF} of the studied samples are higher than the thresholds of highly productive upwelling zones (Figure 4).

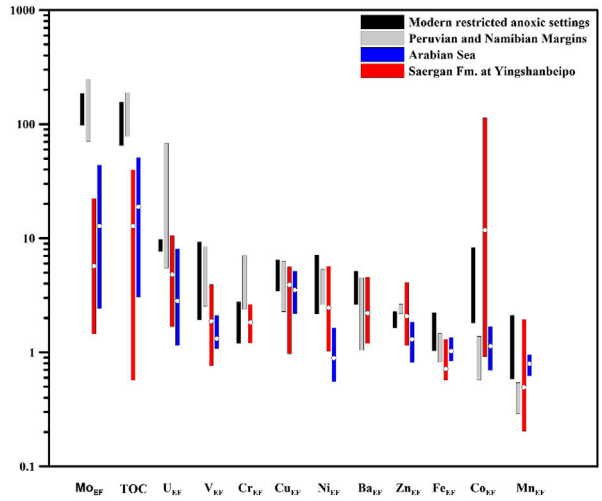

FIGURE 6
Elemental enrichment patterns of the Saergan Formation at Yingshanbeipo section (after Brumsack, 2006). Data of the highly productive Peru and Nambian margins are from Brumsack (2006). Data of the Arabian Sea are from Van der Weijden et al. (2006). The open circles within the red and the blue bars show the average values of the elemental enrichment factors. Note all the enrichments factor are normalized to the average shale (Wedepohl, 1991) in order to conform to Brumsack (2006).

As Cd data are not available for our samples, we calculated the Cd/Mo ratios of the adjacent Dawangou section (Liu M. et al., 2019). Most Dawangou samples are characterized by Cd/Mo ratios <0.1, and Cd/Mo >0.1 are only found in samples with extremely low Mo (Mo <1 ppm), indicating Mo inventory in these samples is dominated by detrital but authigentic Mo. Collectively, the Co*Mn and Cd/Mo data of the Saergan Formation in the Keping region are inconsistent with that of highly productive upwelling settings but more resemble that of upwelling zones with less pronounced OMZs or settings that features both upwelling and restriction.

In Figure 6, the elemental enrichment factors pattern of our sample set shows distinct characteristics compared to both highly productive upwelling zones and anoxic restricted basins, notably in terms of the Mo, U, V, and TOC values. In contrast, the elemental data are more comparable to that of the Arabian Sea characterized by a less pronounced OMZ and moderate enrichments in Mo, U, V, and TOC. However, the Mn and Co data of the Yingshanbeipo samples cover a wide range, with some samples exhibiting high Co_{EF} and Mn_{EF} values typical of anoxic restricted basins. We consider basin restriction is an unlikely explanation for the high Co_{EF} and Mn_{EF} values. First, the high Co_{EF} and Mn_{EF} values are found to be within the interval where the inferred maximum flooding surface is located (Figure 2). Elevated sea level in restricted settings would result in better connectivity to the open ocean and improved circulation, which is not optimal for the accumulation of aqueous Co and Mn in restricted settings (see discussion above), contradicting the high Co_{EF} and Mn_{EF} values. Secondly, the Mo-U patterns of the Yingshanbeipo samples were plotted along the open ocean trend (Figure 5), suggesting no significant basin restriction during the deposition of the samples. We consider the

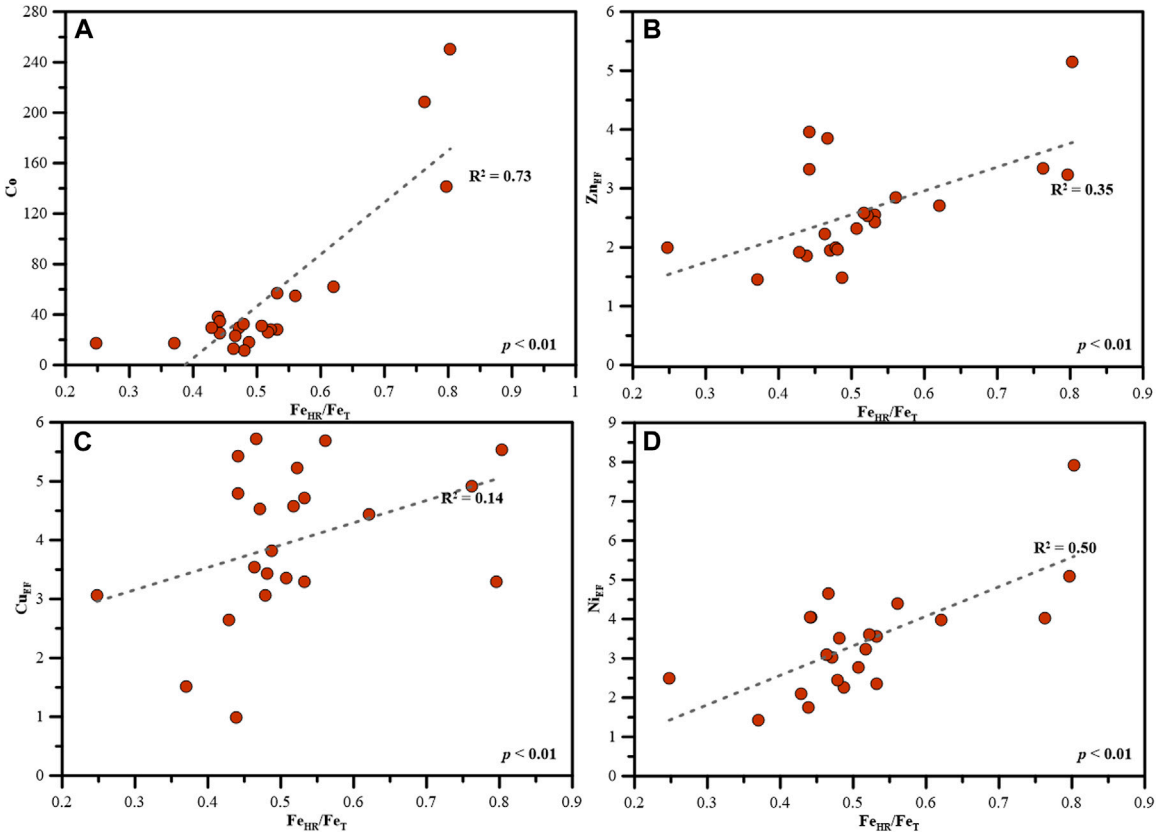

FIGURE 7
Co-Fe_{HR}/Fe_T **(A)**, Zn_{EF}-Fe_{HR}/Fe_T **(B)**, Cu_{EF}-Fe_{HR}/Fe_T **(C)** and Ni_{EF}-Fe_{HR}/Fe_T **(D)** diagrams of the Saergan Formation in the Yingshanbeipo Section.

high Co_{EF} and Mn_{EF} values in this interval may have largely been resulted from increased anoxia. As Co is known to form insoluble sulfide in anoxic waters (Huerta-Diaz and Morse, 1992), the high Co_{EF} values are likely to have resulted from an increase in anoxia of bottom waters, as indicated by concurrent high Co_{EF} and Fe_{HR}/Fe_T ratios and the positive correlation between Co and Fe_{HR}/Fe_T values (Figure 2; Figure 7). Increase in anoxia would have enhanced the H_2S production in pore waters, thus promoting Co take-up in sediments. For Mn, the higher Mn_{EF} may link to several mechanisms: 1) the remobilization of Mn from shallow, oxic/suboxic shelf during the expansion of anoxia and transgression represents an external source of aqueous Mn in seawaters; 2) The increase in anoxia of bottom waters would enhance the alkalinity via intensified OM degradation, resulting in Mn-bearing carbonate precipitation (Lenz et al., 2015a; 2015b).

To summarize, although the Saergan Formation in the Keping area was likely to have been deposited in a protected setting, our data indicate it had a good connection to the open ocean. The elemental features of this organic-rich interval are suggestive of an upwelling setting. However, the OMZ where the Saergan Formation had developed may have been less pronounced than those of Peru and Namibian margins with strong perennial upwelling. The less pronounced OMZ indicates in the upwelling system in NW Tarim was transient similar to the modern Arabian Sea, or less intense upwelling rates of deep waters.

5.4 Primary productivity and OM accumulation

Trace metals like Cu, Ni, and Zn have been considered as robust proxies in tracking primary productivity in marine settings (e.g., Tribovillard et al., 2006; Piper and Calvert, 2009; Zhang et al., 2018). These metals behave as micronutrients in oxic marine environment. Biological uptake or complexation with organic ligands can result in the acceleration scavenging of the metals in the water column. Consequently, settling OM represents an important path for transferring the metals into marine sediments (Algeo and Maynard, 2004; Böning et al., 2004; Tribovillard et al., 2006). Upon OM degradation, the metals are liberated into pore water and further incorporated in pyrite or precipitated as their own sulfides (Morse and Luther, 1999; Tribovillard et al., 2006). On the other hand, bottom-water redox conditions may also exert an important influence on the accumulation of the metals as they are known to be reactive to H_2S (e.g., Algeo and Maynard, 2004; little et al., 2015).

As shown in Figure 6, the $Ni_{EF,}$ and Zn_{EF} of the Saergan Formation are located between the ranges of the Peru and Namibian margins and the Arabian Sea, while the Cu_{EF} shows comparable values. The data indicate moderate to high productivity, consistent with our inference of a less pronounced OMZ when compared to the highly productive Peru and the Namibian margins.

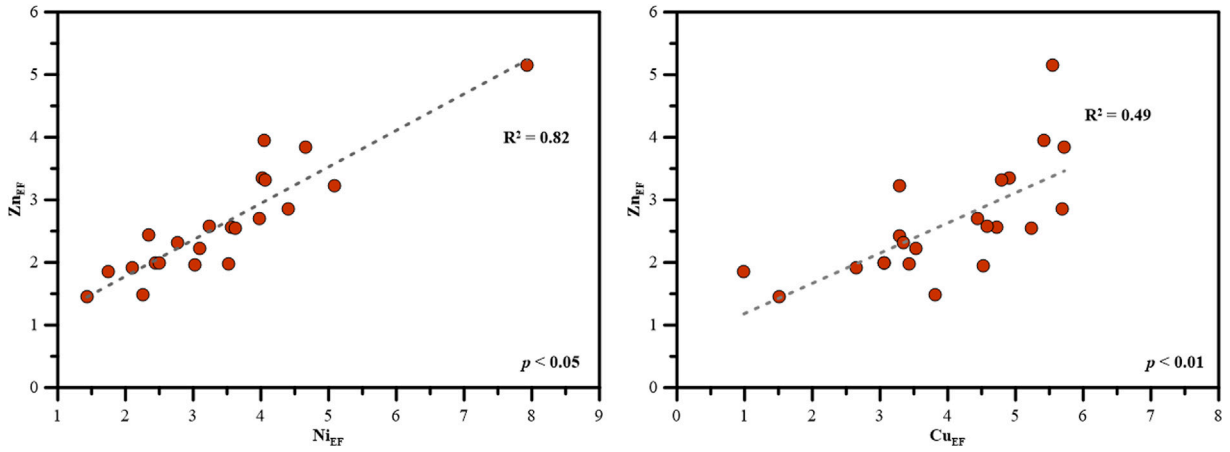

FIGURE 8
Zn_{EF}-Ni_{EF} and Cu_{EF}-Zn_{EF} diagrams of the Saergan Formation in the Yingshanbeipo Section.

In Figure 8, The R^2 are 0.82 for Ni_{EF} vs. Zn_{EF} (p <0.05) and 0.49 for Cu_{EF} vs. Zn_{EF} (p <0.01), respectively. The good correlations observed here indicate the metals originated from similar sources, consistent with settling with OM as the dominating origin of the micronutrients in productive settings. As mentioned above, enrichments of the metals may also be promoted via reducing bottom waters. However, the generally poor correlations between Cu_{EF}, Ni_{EF}, and Zn_{EF} values and Fe_{HR}/Fe_T (R^2 = 0.14, 0.50, and 0.35, respectively, all p values <0.01; Figure 7) imply that redox conditions may have exerted only a secondary influence on the enrichments of the metals. Therefore, our data reveal that productivity was the dominating factor that controlled the micronutrients and OM accumulations in the Saergan Formation.

The vertical profiles of the micro-nutrients, TOC and Fe_{HR}/Fe_T also support that productivity was the more important controlling factor of Ni, Cu, Zn, and OM accumulation. As shown in Figure 2, the profile TOC mimics closely that of Ni_{EF}, Cu_{EF}, and Zn_{EF} through most of the Saergan Formation while the Fe_{HR}/Fe_T ratios exhibit a different pattern (Figure 2). The only exception is the interval in the middle Saergan Formation that characterized by pronounced peaks in Fe_{HR}/Fe_T ratios (shaded area in Figure 2). For this interval, dramatic increases are observed in both Ni, Cu, and Zn enrichments and Fe_{HR}/Fe_T ratios, but not for TOC. Moreover, the peaks in the metals and Fe_{HR}/Fe_T values are found to correspond to relatively low TOC values. The lack of prominent increase in TOC values indicates the benthic redox condition but productivity was the key factor for the micro-nutrient enrichments for this interval.

5.5 Depositional model of the Saergan Formation

Deposition of the Saergan Formation spans a time interval from middle Darriwilian to early Sandbian, a period that witnessed profound changes in environmental conditions (Stigall et al., 2019 and references therein). $\delta^{18}O$ records of conodonts with high temporal resolution reveal a cooling trend from Middle-Late Darriwilian, which may persist into the early Sandbian (Albanesi et al., 2020). This trend is consistent with CIA data from an adjacent section, which indicate an overall cooling in the climate when the Saergan Formation was deposited (Liu M. et al., 2019). Moreover, geochemical proxies indicate intense volcanism for the basal Saergan Formation, which lead to a relatively warmer climate and ample supply of nutrients to the marine system during the deposition of the basal Saergan Formation (Liu M. et al., 2019). These environmental changes, along with sea-level variations, led to changes in the primary productivity, development of bottom water redox dynamics, and the deposition of the organic-rich Saergan Formation in the Keping area, northwest Tarim.

The lower Saergan Formation is characterized by a sudden increase in TOC, micro-nutrients (Ni, Cu, Zn), and redox-sensitive metals enrichments, accompanied by elevated Fe_{HR}/Fe_T values (Figure 2). The data indicate both increasing in primary productivity and the development of anoxia in bottom water conditions, which may link to the combination of enhanced nutrients delivery and rise in relative sea-level. An increase in nutrients supply to marine settings via higher weathering rates (Liu M. et al., 2019) would fuel primary productivity in the photic zone, enhance respiratory oxygen demand and further, expand the OMZ along continental margins (e.g., Wang et al., 2018). Consequently, the shoaling of the redox chemocline, along with the rise in sea-level would favor the impingent of anoxic waters to shallower depths (Figure 9). Finally, anoxia in bottom waters would promote nutrients regenerations and maintain high productivity in the photic zone through the "productivity-anoxia feedback" mechanism (Ingall et al., 1993).

During deposition of the middle Saergan Formation, the transition to a cooler climate would have reduced the nutrients supply by weathering. The cooler climate, on the other hand, would intensify upwelling and nutrients recycling, thus maintaining productivity. At the top of this part, dramatic increases are observed in both micro-nutrient enrichments and Fe_{HR}/Fe_T ratios, but not for TOC, indicating intensified bottom water

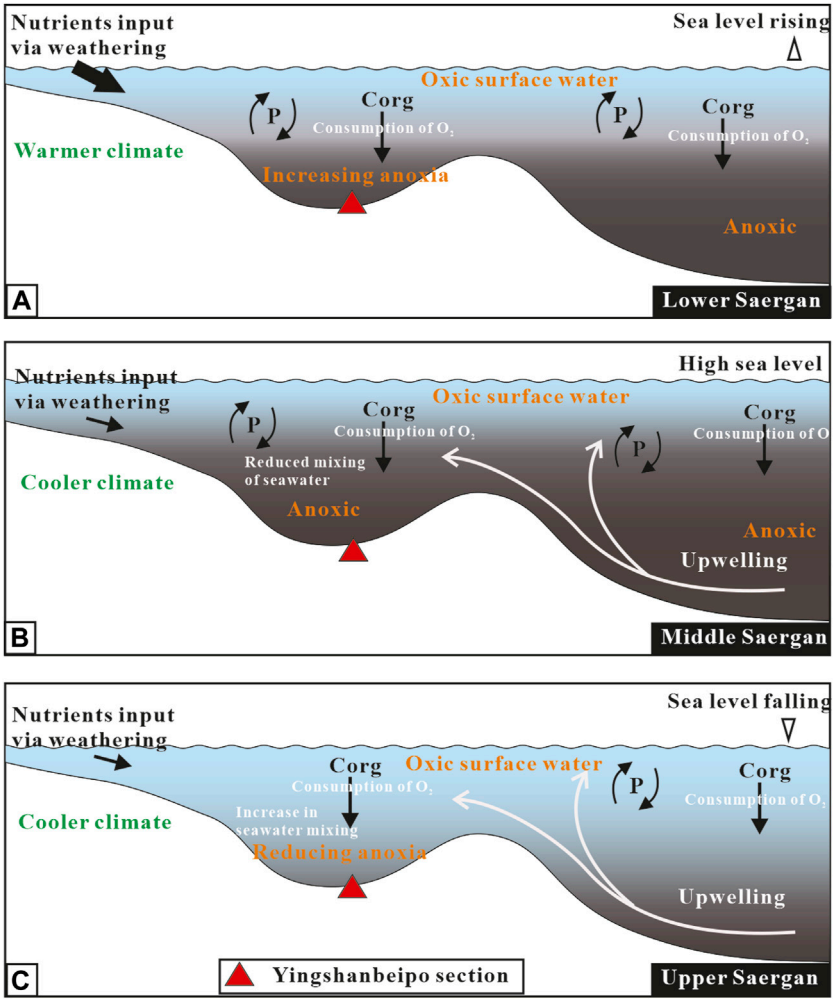

FIGURE 9
Schematic illustrations to show the depositional models of the lower **(A)**, the middle **(B)** and the upper **(C)** parts of the Saergan Formation, respectively.

anoxia was not triggered by a rise in productivity. The maximum in anoxia, which corresponds to the inferred maximum flooding surface (section 2), may link to the reduced mixing from oxic surface waters at high sea levels (e.g., Harris et al., 2018; Figure 9).

For the rest of the Saergan, Fe_{HR}/Fe_T remains invariant in the lower part, followed by a decrease in the upper part. The overall TOC is slightly elevated compared to that of the middle part despite the decrease in reducing conditions, indicating an increase in productivity. The persisting cooling in climate is a plausible explanation for the increase. On the other hand, the increase may also be a reflection of the offshore productivity gradient: offshore waters are less productive compared to the nearshore waters in upwelling zones (e.g., Suess et al., 1987). Therefore, regression in the upper Saergan Formation would have decreased the offshore distance of the Keping area and shifted the area towards the more productive coast, increasing productivity. Meanwhile, along with the decrease in relative sea-level through time, more oxygenated conditions in bottom waters resumed at the topmost Saergan Formation as a result of enhanced mixing from oxic surface waters (Figure 9).

6 Conclusion

Based on multiple geochemical proxies (Iron speciation, major and trace elements, and TOC), we reconstructed the paleoenvironmental conditions for the black shales of the Ordovician Saergan Formation at Yinghsnbeipo section, northwest Tarim Basin. The following findings were obtained:

The Saergan Formation was likely developed in an ancient upwelling zone that was less productive than the modern Peru and Namibian margins. During deposition, there was a strong connection between the water mass and the open ocean. Bottom waters were characterized by varying redox conditions, evolving from suboxic to anoxic conditions at its basal part, displaying maximum anoxia in the middle, and returning to suboxic

conditions at its top. The accumulation of organic matter within the unit was manipulated by a combination of environmental changes including relative sea-level fluctuations, nutrient supply, and oceanic circulation impacted by climate changes.

Data availability statement

The original contributions presented in the study are included in the article/Supplementary Material, further inquiries can be directed to the corresponding authors.

Author contributions

BZ: Conceptualization, Writing–original draft. TG: Data curation, Funding acquisition, Writing–original draft. CL: Data curation, Methodology, Writing–review and editing. WP: Investigation, Writing–review and editing. YC: Investigation, Writing–review and editing. YZ: Investigation, Writing–review and editing. TY: Conceptualization, Funding acquisition, Writing–review and editing.

Funding

The author(s) declare financial support was received for the research, authorship, and/or publication of this article. This project was financially supported by the National Science and Technology Major Project of China (No. 2016ZX05004-004), the Fundamental Research Funds for the Central Universities (No. B200202009), and the Strategic Priority Research Program (B) of the Chinese Academy of Sciences (CAS) (No. XDB26000000).

Acknowledgments

We thank Miss Liu Yang for her help in the lab. We thank TH and LT for their detailed and helpful remarks that helped in improving the presentation of the data.

Conflict of interest

Authors WP and YC were employed by Tarim Oil Field Company, PetroChina.

The remaining authors declare that the research was conducted in the absence of any commercial or financial relationships that could be construed as a potential conflict of interest.

Publisher's note

References

Albanesi, G. L., Barnes, C. R., Trotter, J. A., Williams, I. S., and Bergstrom, S. M. (2020). Comparative Lower-Middle Ordovician conodont oxygen isotope palaeothermometry of the Argentine Precordillera and Laurentian margins. *Palaeogeogr. Palaeoclimatol. Palaeoecol.* 549, 109115. doi:10.1016/j.palaeo.2019.03.016

Algeo, T. J., and Li, C. (2020). Redox classification and calibration of redox thresholds in sedimentary systems. *Geochim. Cosmochim. Acta* 287, 8–26. doi:10.1016/j.gca.2020.01.055

Algeo, T. J., and Maynard, J. B. (2004). Trace-element behavior and redox facies in core shales of Upper Pennsylvanian Kansas-type cyclothems. *Chem. Geol.* 206, 289–318. doi:10.1016/j.chemgeo.2003.12.009

Algeo, T. J., and Tribovillard, N. (2009). Environmental analysis of paleoceanographic systems based on molybdenum–uranium covariation. *Chem. Geol.* 268, 211–225. doi:10.1016/j.chemgeo.2009.09.001

Bergström, S. M., Finney, S. C., Chen, X., Palsson, C., Wang, Z.-H., and Grahn, Y. (2000). A proposed global boundary stratotype for the base of the upper series of the ordovician system: the fågelsång section, scania, southern Sweden. *Episodes* 23, 102–109. doi:10.18814/epiiugs/2000/v23i2/003

Böning, P., Brumsack, H. J., Böttcher, M. E., Schnetger, B., Kriete, C., Kallmeyer, J., et al. (2004). Geochemistry of Peruvian near-surface sediments. *Geochim. Cosmochim. Acta.* 68, 4429–4451. doi:10.1016/j.gca.2004.04.027

Bruland, K. W. (1980). Oceanographic distributions of cadmium, zinc, nickel, and copper in the North Pacific. *Earth Planet Sc. Lett.* 47, 176–198. doi:10.1016/0012-821x(80)90035-7

Brumsack, H. J. (2006). The trace metal content of recent organic carbon-rich sediments: implications for Cretaceous black shale formation. *Palaeogeogr. Palaeoclimatol. Palaeoecol.* 232, 344–361. doi:10.1016/j.palaeo.2005.05.011

Calvert, S. E., and Price, N. B. (1983). "Geochemistry of Namibian shelf sediments," in *Coastal upwelling; its sediment record*. Editors E. Suess and J. Thiede (Berlin, Germany: Springer), 337–375.

Chen, X., Bergström, S. M., Finney, S. C., Zhang, Y. D., Fan, J. X., Chen, Q., et al. (2017). *Darriwilian to sandbian (ordovician) graptolites from northwest China*. Amsterdam, Netherlands: Elsevier.

Chen, X., Zhang, Y. D., Yue, L., Fan, J. X., Tang, P., Chen, Q., et al. (2012). Biostratigraphic correlation of the Ordovician black shales in Tarim Basin and its peripheral regions. *Sci. China Earth Sci.* 55, 1230–1237. doi:10.1007/s11430-012-4448-6

Clarkson, M. O., Poulton, S. W., Guilbaud, R., and Wood, R. A. (2014). Assessing the utility of Fe/Al and Fe-speciation to record water column redox conditions in carbonate-rich sediments. *Chem. Geol.* 382, 111–122. doi:10.1016/j.chemgeo.2014.05.031

Conway, T. M., and John, S. G. (2015). Biogeochemical cycling of cadmium isotopes along a high-resolution section through the North Atlantic Ocean. *Geochim. Cosmochim. Acta.* 148, 269–283. doi:10.1016/j.gca.2014.09.032

Demaison, G. J., and Moore, G. T. (1980). Anoxic environments and oil source bed genesis. *Org. Geochem.* 2, 9–31. doi:10.1016/0146-6380(80)90017-0

Ding, H., Yao, S., and Chen, J. (2014). Authigenic pyrite formation and re-oxidation as an indicator of an unsteady-state redox sedimentary environment: evidence from the intertidal mangrove sediments of Hainan Island, China. *Con. Shelf Res.* 78, 85–99. doi:10.1016/j.csr.2014.02.011

Edwards, C. T., Saltzman, M. R., Royer, D. L., and Fike, D. A. (2017). Oxygenation as a driver of the great ordovician biodiversification event. *Nat. Geosci.* 10, 925–929. doi:10.1038/s41561-017-0006-3

Erickson, B. E., and Helz, G. R. (2000). Molybdenum(VI) speciation in sulfidic waters: . *Geochim. Cosmochim. Acta.* 64, 1149–1158. doi:10.1016/s0016-7037(99)00423-8

Gao, H., He, D. F., Tong, X. G., Wen, Z. X., Wang, Z. M., and He, J. Y. (2016). Tectonic-depositional environment and proto-type basins during the depositional period of middle ordovician yijianfang Formation in Tarim Basin. *J. Palaeogeogr.* 18 (6), 986–1001. (in Chinese with English abstract). doi:10.7605/gdlxb.2016.06.075

Gao, P., Li, S., Lash, G. G., Yan, D., and Xiao, X. (2021). Stratigraphic framework, redox history, and organic matter accumulation of an Early Cambrian intraplatfrom basin on the Yangtze Platform, South China. *Mar. Pet. Geol.* 130, 105095. doi:10.1016/j.marpetgeo.2021.105095

Gao, Z. Y., Zhang, S. C., Li, J. J., Zhang, B. M., Fu, Q. Y., and Lu, Y. H. (2010). Distribution and sedimentary environments of salgan and yingan shales of the middle-

upper ordovician in western Tarim Basin. *J. Palaeogeogr.* 12 (5), 599–608. (in Chinese with English abstract). doi:10.7605/gdlxb.2010.05.009

Gao, Z. Y., Zhang, S. C., Liu, H., Li, J. J., Zhang, B. M., Gu, Q. Y., et al. (2012). Relationship between high-frequency sea-level changes and organic matter of Middle-Upper Ordovician marine source rocks from the Dawangou section in the Keping area,Xinjiang. *Acta Petrol. Sin.* 33 (2), 232–240. in Chinese with English abstract. doi:10.7623/syxb201202007

Harris, N. B., McMillan, J. M., Knapp, L. J., and Mastalerz, M. (2018). Organic matter accumulation in the upper devonian duvernay formation, western Canada sedimentary basin, from sequence stratigraphic analysis and geochemical proxies. *Sediment. Geol.* 376, 185–203. doi:10.1016/j.sedgeo.2018.09.004

He, T. H., Li, W. H., Lu, S. F., Yang, E. Q., Jing, T. T., Ying, J. F., et al. (2023). Quantitatively unmixing method for complex mixed oil based on its fractions carbon isotopes: a case from the Tarim Basin, NW China. *Pet. Sc.* 20, 102–113. doi:10.1016/j.petsci.2022.07.010

Helz, G. R., Miller, C. V., Charnock, J. M., Mosselmans, J. F. W., Pattrick, R. A. D., Garner, C. D., et al. (1996). Mechanism of molybdenum removal from the sea and its concentration in black shales: EXAFS evidence. *Geochim. Cosmochim. Acta.* 60, 3631–3642. doi:10.1016/0016-7037(96)00195-0

Huerta-Diaz, M. A., and Morse, J. W. (1990). A quantitative method for determination of trace metal concentrations in sedimentary pyrite. *Mar. Chem.* 29, 119–144. doi:10.1016/0304-4203(90)90009-2

Huerta-Diaz, M. A., and Morse, J. W. (1992). Pyritization of trace metals in anoxic marine sediments. *Geochim. Cosmochim. Acta.* 56 (7), 2681–2702. doi:10.1016/0016-7037(92)90353-k

Ingall, E. D., Bustin, R. M., and Van Cappellen, P. (1993). Influence of water column anoxia on the burial and preservation of carbon and phosphorus in marine shales. *Geochim. Cosmochim. Acta.* 57, 303–316. doi:10.1016/0016-7037(93)90433-w

Jia, C. Z., Wang, L. S., Wei, G. Q., Chen, H. L., Jia, D., Guo, Z. J., et al. (2004). *Tectonic evolution and continental dynamics of Tarim Basin*. Beijign: Petroleum Industry Press.

Jin, C., Li, C., Peng, X., Cui, H., Shi, W., Zhang, Z., et al. (2014). Spatiotemporal variability of ocean chemistry in the early Cambrian, South China. *Sci. China-Earth Sci.* 57, 579–591. doi:10.1007/s11430-013-4779-y

Krause, A. J., Mills, B. J. W., Zhang, S., Planavsky, N. J., Lenton, T. M., and Poulton, S. W. (2018). Stepwise oxygenation of the Paleozoic atmosphere. *Nat. Commun.* 9, 4081. doi:10.1038/s41467-018-06383-y

LaGrange, M. T., Konhauser, K. O., Catuneanu, O., Harris, B. S., Playter, T. L., and Gingras, M. K. (2020). Sequence stratigraphy in organic-rich marine mudstone successions using chemostratigraphic datasets. *Earth Sci. Rev.* 203, 103137. doi:10.1016/j.earscirev.2020.103137

Lenz, C., Jilbert, T., Conley, D. J., and Slomp, C. P. (2015a). Hypoxia-driven variations in iron and manganese shuttling in the Baltic Sea over the past 8 kyr. *Geochem. Geophy., Geosyst.* 16, 3754–3766. doi:10.1002/2015gc005960

Lenz, C., Jilbert, T., Conley, D. J., Wolthers, M., and Slomp, C. P. (2015b). Are recent changes in sediment manganese sequestration in the euxinic basins of the Baltic Sea linked to the expansion of hypoxia? *Biogeosciences* 12, 4875–4894. doi:10.5194/bg-12-4875-2015

Li, C., Zhang, J., Li, W., Botting, J., Chen, Q., Fan, J., et al. (2021). Multiple glacio-eustatic cycles and associated environmental changes through the Hirnantian (Late Ordovician) in South China. *Glob. Planet. Change* 207, 103668. doi:10.1016/j.gloplacha.2021.103668

Li, F., Lü, X., Chen, J., Wang, R., Wang, Y., and Chen, Z. (2022). Palaeo-environmental evolution and organic matter enrichment of Eopalaeozoic shales, northwestern Tarim Basin, China: integrated organic and inorganic geochemistry approach. *Palaeogeogr. Palaeoclimatol. Palaeoecol.* 601, 111123. doi:10.1016/j.palaeo.2022.111123

Liang, D. G., Zhang, S. C., Zhang, B. M., and Wang, F. Y. (2000). Understanding on marine oil generation in China based on Tarim Basin. *Earth Sci. Front.* 7 (4), 534–547. (in Chinese with English abstract).

Lin, C., Yang, H., Liu, J., Rui, Z., Cai, Z., Li, S., et al. (2012). Sequence architecture and depositional evolution of the Ordovician carbonate platform margins in the Tarim Basin and its response to tectonism and sea-level change. *Basin Res.* 24, 559–582. doi:10.1111/j.1365-2117.2011.00536.x

Liu, C., Jiang, S. Y., Su, X., Huang, C. Y., Yang, T., Bian, X., et al. (2019a). An effective method to distinguish between artificial and authigenic gypsum in marine sediments. *Mar. Pet. Geol.* 110, 706–716. doi:10.1016/j.marpetgeo.2019.07.044

Liu, M., Chen, D., Zhou, X., Yuan, W., and Liu, L. (2019b). Climatic and oceanic changes during the middle-late ordovician transition in the Tarim Basin, NW China and implications for the great ordovician biodiversification event. *Palaeogeogr. Palaeoclimatol. Palaeoecol.* 514, 522–535. doi:10.1016/j.palaeo.2018.10.032

Lu, Y., Jiang, S., Lu, Y., Xu, S., and Wang, Y. (2019). Productivity or preservation? The factors controlling the organic matter accumulation in the late Katian through Hirnantian Wufeng organic-rich shale, South China. *Mar. Pet. Geol.* 109, 22–35. doi:10.1016/j.marpetgeo.2019.06.007

Lumiste, K., Mänd, K., Bailey, J., Stüeken, E. E., Paiste, K., Lang, L., et al. (2021). Constraining the conditions of phosphogenesis: stable isotope and trace element systematics of Recent Namibian phosphatic sediments. *Geochim. Cosmochim. Acta* 302, 141–159. doi:10.1016/j.gca.2021.03.022

Lyons, T. W., and Severmann, S. (2006). A critical look at iron paleoredox proxies: new insights from modern euxinic marine basins. *Geochim. Cosmochim. Acta.* 70, 5698–5722. doi:10.1016/j.gca.2006.08.021

Ma, A. L., Jin, Z. Y., Zhang, S. C., and Wang, Y. (2020). Molecular geochemical characteristics of Camrbian-Ordovician source rocks in Tarims Basin, NW China. *Geochimica* 35 (6), 593–601. in Chinese with English abstract. doi:10.11764/j.issn.1672-1926.2019.08.005

Ma, L., Zhang, Z. L., Wang, G., and Li, Y. (2013). Microfacies of the carbonates and palaeogeography of the Saergan Formation (Middle–Upper ordovician), kalpin stratigraphic region, Tarim, NW China. *Acta micropalaeontol. Sin.* 30 (4), 344–352. in Chinese with English abstract.

Ma, P., Dong, C., and Lin, C. (2022). Petrographic and geochemical characteristics of nodular carbonate-bearing fluorapatite in the lacustrine shale of the shahejie formation, dongying depression, bohai bay basin. *Sediment. Geol.* 439, 106218. doi:10.1016/j.sedgeo.2022.106218

Morford, J. L., and Emerson, S. (1999). The geochemistry of redox sensitive trace metals in sediments. *Geochim. Cosmochim. Acta.* 63, 1735–1750. doi:10.1016/s0016-7037(99)00126-x

Morse, J. W., and Luther, G. W. (1999). Chemical influences on trace metal-sulfide interactions in anoxic sediments. *Geochim. Cosmochim. Acta.* 63, 3373–3378. doi:10.1016/s0016-7037(99)00258-6

Munnecke, A., Zhang, Y., Liu, X., and Cheng, J. (2011). Stable carbon isotope stratigraphy in the Ordovician of South China. *Palaeogeogr. Palaeoclimatol. Palaeoecol.* 307, 17–43. doi:10.1016/j.palaeo.2011.04.015

Pedersen, T. F., and Calvert, S. E. (1990). Anoxia vs. productivity: what controls the formation of organic-carbon-rich sediments and sedimentary rocks? *AAPG Bull.* 74, 454–466. doi:10.1306/0c9b232b-1710-11d7-8645000102c1865d

Peng, M., Ma, D., Tian, J., Zhang, X., and Li, J. (2023). Paleoenvironmental changes during the middle-late ordovician transition, northwestern Tarim Basin, NW China and implications for the great ordovician biodiversification event. *J. Asian Earth Sci.* 242, 105462. doi:10.1016/j.jseaes.2022.105462

Piper, D. Z., and Calvert, S. E. (2009). A marine biogeochemical perspective on black shale deposition. *Earth Sci. Rev.* 95, 63–96. doi:10.1016/j.earscirev.2009.03.001

Poulton, S. W., and Canfield, D. E. (2005). Development of a sequential extraction procedure for iron: implications for iron partitioning in continentally derived particulates. *Chem. Geol.* 214, 209–221. doi:10.1016/j.chemgeo.2004.09.003

Poulton, S. W., and Canfield, D. E. (2011). Ferruginous conditions: a dominant feature of the ocean through earth's history. *Elements* 7, 107–112. doi:10.2113/gselements.7.2.107

Raiswell, R., and Canfield, D. E. (1998). Sources of iron for pyrite formation in marine sediments. *Am. J. Sci.* 298, 219–245. doi:10.2475/ajs.298.3.219

Rimmer, S., Thompson, J., Goodnight, S., and Robl, T. (2004). Multiple controls on the preservation of organic matter in Devonian–Mississippian marine black shales: geochemical and petrographic evidence. *Palaeogeogr. Palaeoclimatol. Palaeoecol.* 215, 125–154. doi:10.1016/s0031-0182(04)00466-3

Sageman, B. B., Murphy, A. E., Werne, J. P., Ver Straeten, C. A., Hollander, D. J., and Lyons, T. W. (2003). A tale of shales: the relative roles of production, decomposition, and dilution in the accumulation of organic-rich strata, Middle-Upper Devonian, Appalachian basin. *Chem. Geol.* 195, 229–273. doi:10.1016/s0009-2541(02)00397-2

Sarmiento, J. L., and Gruber, N. (2006). *Ocean biogeochemical dynamics*. New Jersey, United States: Princeton University Press.

Servais, T., and Harper, D. A. T. (2018). The great ordovician biodiversification event (GOBE): definition, concept and duration. *Lethaia* 51, 151–164. doi:10.1111/let.12259

Stigall, A. L., Edwards, C. T., Freeman, R. L., and Rasmussen, C. (2019). Coordinated biotic and abiotic change during the Great Ordovician Biodiversification Event: Darriwilian assembly of early Paleozoic building blocks. *Palaeogeogr. Palaeoclimatol. Palaeoecol.* 530, 249–270. doi:10.1016/j.palaeo.2019.05.034

Suess, E., Kulm, L. D., and Killingley, J. S. (1987). in *Coastal upwelling and a history of organic-rich mudstone deposition off Peru" in Marine Petroleum Source Rocks*. Editors J. Brooks and A. Fleet (London: Geological Society of London), 181–197.

Sweere, T., van den Boorn, S., Dickson, A. J., and Reichart, G. J. (2016). Definition of new trace-metal proxies for the controls on organic matter enrichment in marine sediments based on Mn, Co, Mo and Cd concentrations. *Chem. Geol.* 441, 235–245. doi:10.1016/j.chemgeo.2016.08.028

Taylor, S. R., and McLennan, S. M. (1985). *The continental crust: its composition and evolution*. Oxford: Blackwell Scientific Publications, 312.

Torsvik, T. H., and Cocks, L. R. M. (2013). in *"New global palaeogeographical reconstructions for the early palaeozoic and their generation" in early palaeozoic biogeography and palaeogeography*. Editors D. A. T. Harper and T. Servais (London: Geological Society of London), 5–24.

Tribovillard, N., Algeo, T. J., Baudin, F., and Riboulleau, A. (2012). Analysis of marine environmental conditions based onmolybdenum-uranium covariation—applications to Mesozoic paleoceanography. *Chem. Geol.* 324-325, 46–58. doi:10.1016/j.chemgeo.2011.09.009

Tribovillard, N., Algeo, T. J., Lyons, T., and Riboulleau, A. (2006). Trace metals as paleoredox and paleoproductivity proxies: an update. *Chem. Geol.* 232, 12–32. doi:10.1016/j.chemgeo.2006.02.012

Trotter, J. A., Williams, I. S., Barnes, C. R., Lecuyer, C., and Nicoll, R. S. (2008). Did cooling oceans trigger Ordovician biodiversification? Evidence from conodont thermometry. *Science* 321, 550–554. doi:10.1126/science.1155814

Turner, B. W., Treanton, J. A., and Slatt, R. M. (2016). The use of chemostratigraphy to refine ambiguous sequence stratigraphic correlations in marine mudrocks. An example from the Woodford Shale, Oklahoma, USA. *J. Geol. Soc.* 173, 854–868. doi:10.1144/jgs2015-125

Tyson, R. V. (2005). in *The "productivity versus preservation" controversy: cause, flaws, and resolution" in Deposition of organic-carbon-rich sediments:models mechanisms, and consequences*. Editor N. B. Harris (Claremore: SEPM Special Publication), 17–33.

Van der Weijden, C., Reichart, G. J., and Os, B. (2006). Sedimentary trace element records over the last 200 kyr from within and below the northern Arabian Sea oxygen minimum zone. *Mar. Geol.* 231, 69–88. doi:10.1016/j.margeo.2006.05.013

Wang, D., Ling, H. F., Struck, U., Zhu, X. K., Zhu, M., He, T., et al. (2018). Coupling of ocean redox and animal evolution during the Ediacaran-Cambrian transition. *Nat. Commun.* 9, 2575. doi:10.1038/s41467-018-04980-5

Webby, B. D., Paris, F., Droser, M. L., and Percival, I. G. (2004). *The Great ordovician biodiversification event*. New York: Columbia University Press.

Wedepohl, K. H. (1991). ""The composition of the upper earth's crust and the natural cycles of selected metals" in Metals in natural raw materials," in *Natural resources. Metals and their compounds in the environment*. Editor E. Merian (Weinheim: VCH), 3–17.

Wijsman, J. W. M., Middelburg, J. J., and Heip, C. H. R. (2001). Reactive iron in Black Sea Sediments: implications for iron cycling. *Mar. Geol.* 172, 167–180. doi:10.1016/s0025-3227(00)00122-5

Yang, X., Li, Z., Fan, T., Gao, Z., and Tang, S. (2020). Carbon isotope (δ^{13} C_{carb}) stratigraphy of the Early–Middle Ordovician (Tremadocian–Darriwilian) carbonate platform in the Tarim Basin, NW China: implications for global correlations. *Geol. Mag.* 158, 487–508. doi:10.1017/s0016756820000643

Zhang, B., Yao, S., Wignall, P. B., Hu, W., Ding, H., Liu, B., et al. (2018). Widespread coastal upwelling along the eastern paleo-tethys margin (south China) during the middle permian (guadalupian): implications for organic matter accumulation. *Mar. Pet. Geol.* 97, 113–126. doi:10.1016/j.marpetgeo.2018.06.025

Zhang, Y., and Munnecke, A. (2016). Ordovician stable carbon isotope stratigraphy in the Tarim Basin, NW China. *Palaeogeogr. Palaeoclimatol. Palaeoecol.* 458, 154–175. doi:10.1016/j.palaeo.2015.09.001

Zhao, Z. J., Zhao, Z. X., and Huang, Z. B. (2006). Ordovician conodont zones and sedimentary sequences of the Tarim Basin, Xinjiang, NW China. *J. Stratigr.* 30 (3), 193–203. in Chinese with English abstract.

Zhen, Y. Y., Wang, Z. H., Zhang, Y. D., Bergström, S. M., Percival, I. G., and Chen, J. F. (2011). Middle to late ordovician (Darriwilian–Sandbian) conodonts from the Dawangou section, kalpin area of the Tarim Basin, northwestern China. *Rec. Aus. Mus.* 63 (3), 203–266. doi:10.3853/j.0067-1975.63.2011.1586